Adsorption (2022) 28:27–39
https://doi.org/10.1007/s10450-021-00350-8

Absolute adsorption and adsorbed volume modeling for supercritical methane adsorption on shale

Ke Hu[1] · **Helmut Mischo**[1]

Received: 24 July 2020 / Revised: 10 October 2021 / Accepted: 25 November 2021 / Published online: 9 March 2022

Abstract
Adsorbed methane significantly affects shale gas reservoir estimates and shale gas transport in shale formations. Hence, a practical model for accurately representing methane adsorption behavior at high-pressure and high-temperature in shale is imperative. In this study, a reliable mathematical framework that estimates the absolute adsorption directly from low-pressure excess adsorption data is applied to describe the excess methane adsorption data in literature. This method provides detailed information on the volume and density of adsorbed methane. The obtained results indicate that the extensively used supercritical Dubinin-Radushkevich model with constant adsorbed phase density underestimates absolute adsorption at high pressure. The adsorbed methane volume increases both the pressure and expands with the temperature. The adsorbed methane density reduces above 10 MPa, and approaches a steady value at high pressure. This study provides a novel method for estimating adsorbed shale gas, which is expected improve the prediction of shale gas in place and gas production.

Keywords Shale gas · Methane adsorption · Absolute adsorption · Supercritical

1 Introduction

The rapidly increasing production of shale gas due to the advances in horizontal drilling and multistage hydraulic fracturing techniques has attracted growing interest in recent years [1]. In 2019, dry shale gas production accounted for 75% of the U.S. natural gas production, and this value is expected to exceed 90% in 2050, according to the Energy Information Administration (2019) [2].

Shale gas can be stored in three states in shale reservoirs: free and compressed gas within pores and fractures, adsorbed gas on the surfaces of organic matter and minerals, and dissolved gas in water and organic matter. Curtis et al. indicated that adsorbed gas accounts for 20%–85% of the total quantity [3]; Montgomery et al. [4] reported that the percentage of adsorbed gas in the total gas in place (GIP) was as high is as 50%–60% in some cases. Hence, it is clear that adsorbed methane constitutes as significant proportion of the total shale gas content. In most shale formations, the burial depth is 2000–4000 m with pressures of up to 25 MPa, and the corresponding temperature can reach 60–100 °C. To evaluate the adsorption of methane on shales, a series of isothermal adsorption experiments were performed under different conditions (see Table 1).

All the commonly used models for high-pressure methane adsorption are based either on the empirical monomolecular layer (e.g., Langmuir-based model) or pore-filling (e.g., D-R-based model) assumption. The Langmuir-based model does not consider the interaction between the adsorbed molecules [14]. The D-R-based model was developed based on the pore filling theory and is only valid for pore diameters below 2 nm [15]. However, numerous investigations have revealed that shale formations include a wide range of pore sizes, from micro- to macropores [16–24].

The aforementioned methods are based on assumptions that the unknown adsorbed phase density remains constant with the changing adsorbed phase volume or that the unknown adsorbed phase volume remains constant with the changing adsorbed phase density [25, 26]. However, molecular dynamics simulations have indicated that the adsorbed phase density is position-dependent in the slit pores and that the adsorbed phase density varies with the increase in pressure [27]. Additionally, the adsorbed phase volume is not constant in ultrahigh-pressure gas adsorption measurements [28, 29, 12]. The hydrostatic pressure

✉ Ke Hu
huke314@gmail.com

[1] Institute of Mining and Special Civil Engineering, TU Bergakademie Freiberg, 09599 Freiberg, Sachsen, Germany

Table 1 Review of recent literature on high pressure methane adsorption on shales

Reference	Pressure	Temperature	Model	Assumption
[5]	25 MPa	65 ℃	Langmuir based	ρ_a constant
[6]	25 MPa	Up to 150 ℃	Langmuir based	ρ_a constant
[7]	about 27 MPa	45 ℃	Langmuir model	none
[8]	35 MPa	Up to 150 ℃	D-R based	ρ_a constant
[9]	27 MPa	Up to 82 ℃	Langmuir based	ρ_a constant
[10]	35 MPa	Up to 120 °C	Langmuir based; D-R based	ρ_a constant
[11]	25 MPa	45 and 130 °C	Langmuir model	ρ_a constant
[12]	60 MPa	Up to140 °C	D-R based	ρ_a constant
[13]	30 MPa	Up to 100 °C	Langmuir based; D-R based	ρ_a constant

in the Upper Ordovician to Lower Silurian shale formations in the Sichuan Basin can reach 60 MPa because the depths can exceed 4000 m [30–32]. Recent advancements in devices based on the gravimetric method have widely facilitated the widespread use of high-pressure and ultra-high-pressure methane adsorption measurements. Li et al. analyzed methane adsorption on Paleozoic shale and kerogen from the Sichuan Basin, and reported that the D-R-based model produced large deviations in the experimental data at 30–60 MPa pressure [12]. Lin et al. performed grand canonical Monte Carlo (GCMC) simulations to describe methane adsorption and desorption on reconstructed shale, and noted that the modified Langmuir model failed to represent ultra-high-pressure data [33].

As a result, neither Langmuir-based not D-R-based models can reflect the physical interpretation of supercritical methane adsorption. Thus, these extensively used models are unsuitable for studying for high-pressure and ultrahigh-pressure methane adsorption. In the last decade, the simplified local density (SLD) model with a specific equation of state (EOS) has been extensively used to represent methane adsorption behaviors in shale [13, 34–37]. However, the SLD model produces relatively large errors at high pressures [13] and is difficult to implement in engineering applications.

Adsorbed gas is another key parameter for predicting the productivity and working life of a producing shale gas well. The absolute adsorption is needed to estimate the shale gas migration in nanopores and to develop a kinetic model [38]. For an accurate evaluation of the isosteric heat of methane adsorption, the adsorbed methane volume is vital [39]. Although several practical methods to determine the absolute adsorption have been proposed [38, 40, 41], however, all of them involve additional experimental procedures. Thus, to improve the understanding of the shale gas storage and migration, an alternative model that can accurately estimate shale gas adsorption (including excess adsorption, absolute adsorption, adsorbed phase volume, and adsorbed phase density) is essential.

The remainder of this study is structured as follows. First, experimental isotherms from the literature were selected and transformed into a Virial plot to obtain Henry's constant. The experimental isotherms were then mathematically converted to generalized isotherms and linearized plots. Next, a model of absolute adsorption was established from the linearized plots. Finally, the estimated volume and density of adsorbed methane, absolute adsorption were compared with the conventional models regarding either volume of adsorbed phase or density of adsorbed phase as an unknown constant.

2 Data acquisition and methodology

2.1 Data acquisition

The data used in this study were measured by Li et al. [10]. using a gravimetric apparatus (ISOSORP-HP Static II, Rubotherm GmbH, Germany). Supercritical methane adsorption was determined at various temperatures (40–120 ℃) and at pressures of up to 35 MPa. Samples FC-47, FC-66, and FC-72, which were drilled at different depth from the Niutitang formation (lower Cambrian) in northeast Guizhou Province were ground into grains of 20–50 mesh for their high-pressure methane adsorption to be investigated. Prior to the methane adsorption, about 5–6 g sample was heated for 12 h at 110 ℃ under approximately 1 kPa to remove the residual gas and moisture. Further details on the samples, including the depth, mineral composition, and pore characteristics, can be found elsewhere [10].

The principal procedures of adsorption measurement are summarized as follows. The methane adsorption was measured at two points: Measurement Point 1 at vacuum ($MP_{1,0}$, including the weight of sample container and shale sample) and experimental condition ($MP_1(\rho,T)$, and the Measurement Point 2 at vacuum ($MP_{2,0}$, including the weight of the titanium sinker, sample container and shale sample) and the experimental condition ($MP_2(\rho,T)$ [42]. The density of bulk methane inside the chamber can be expressed as [43]:

$$\rho_b = \frac{m_{sk,0} - m_{mk}}{V_{sk}} = \frac{\left(MP_{2,0} - MP_{1,0}\right) - \left(MP_2(\rho,T) - MP_1(\rho,T)\right)}{V_{sk}} \tag{1}$$

where the $m_{sk,0}$ and m_{sk} represent the weight of the titanium sinker under vacuum and the experimental condition, respectively, and V_{sk} is the known volume of the titanium sinker. The excess adsorption (n_{ex}), i.e., the difference between the absolute adsorption (n_{abs}) and the amount that would be present in the same volume at the density of the gas in the bulk phase [41], can be expressed as follow according to the Gibbs definition [44]:

$$n_{ex} = \frac{m_a - \rho_b V_a}{Mm_s} = \frac{MP_1(\rho,T) - MP_{1,0} + \rho_b V_0}{Mm_s} \tag{2}$$

where m_a is the absolute amount of adsorbed methane; V_a is the adsorbed phase volume; M is the mole mass of methane; m_s is the weight of the shale sample, and V_0 is the combined volume of the shale sample and sample container. The values of the V_0 and m_s were determined using high pressure helium gravimetry [44].

$$MP_{1,He}(\rho,T) = MP_{1,0} - \rho_{He}V_0 = m_s + m_c - \rho_{He}V_0 \tag{3}$$

where ρ_{He} is the density of Helium, as obtained from Eq. (1), and m_c is the known mass of the sample container. Hence, by plotting the $MP_{1,He}(\rho,T)$ against ρ_{He}, V_0 and m_s can be obtained from the slope and the intercept, respectively. All the right-hand-side terms of Eq. (2) are known. Notably, there is a large deviation between the determined value (0.4524 mg/g) and model-fitted value (0.3703 mg/g) for the first datum of sample FC-66 at 80 ℃ in the original reference. Hence, while evaluating the experimental data in the following sections, this datum was excluded.

2.2 Henry's constant and the virial plot

At relatively low pressure, methane adsorption can be described using Henry's law [45]:

$$n_{abs} = K_H P \tag{4}$$

where K_H is Henry's constant (mmol/MPa) and P is the pressure (MPa).

When the adsorption reaches the equilibrium state, in terms of the virial equation, the absolute uptake n_{abs} and equilibrium pressure P can be expressed as:

$$\ln\left(\frac{P}{n_{abs}}\right) = \frac{1}{T}\sum_i a_i n_{abs}^i + \sum_i b_i n_{abs}^i \tag{5}$$

a_i and b_i are temperature independent parameters. Because Henry's law is valid only at low pressure, the higher order terms in Eq. (5) can be ignored. When the experimental data before the maximum are optimized by the Universal Global Optimization (1stopt, 7d software, http://www.7d-soft.com/en/), the four temperature independent parameters (a_0, a_1, b_0 and b_1) can be achieved (Table 2), and only the points where the difference between excess sorption and absolute sorption is negligible will fall on the smooth curve, as shown in Fig. 1.

To obtain the Henry's constant (K_H), an alternative expression of Eq. (5) was used [46]:

$$\ln\left(\frac{P}{n_{abs}}\right) = \ln\frac{1}{a} + 2C_1 n_{abs} \tag{6}$$

When plot of $\ln(P/n_{abs})$ against n_{abs} was used within the same experimental data which can be well fitted by Eq. (5), a linear relationship is observed for low absolute adsorption values (as shown in Fig. 2 and Table 3); therefore, ln ($1/a$) can be obtained by fitting the curve in this region. Henry's constants obtained at relatively low pressure are then reliable because the difference between the absolute adsorption and excess adsorption in the low-pressure range can be disregarded.

2.3 Evaluation of the absolute from the excess adsorption

Absolute adsorption is the quantity of methane molecules constrained within the shale pore structure. Absolute adsorption is rarely mentioned in the context of methane adsorption at low pressure because absolute and excess adsorption are almost indistinguishable in this case, especially for shales with small adsorption capacity. In case of high-pressure methane adsorption, by contrast, difference between excess and absolute adsorption is considerable, and it is necessary to distinguish them.

The isotherms for methane adsorption under different temperatures can be generalized as a single isotherm by plotting $\ln(1000 \cdot n_{ex})$ against $\ln(K_H \cdot P)$, with P in kPa, as shown in Fig. 3 [47]. To avoid negative results when taking the logarithms, the pressure P as well as the excess adsorption n_{ex} are magnified by a factor of 1000, as depicted in the following figures [48]. As seen in Fig. 3, most of the points in the relatively low methane coverage range are located on a smooth curve, mainly because the difference between

Table 2 The first-order fitting results of parameters in Eq. (5) by fitting data below the maximum

Sample	a_0	a_1	b_0	b_1	RSS
FC-47	−2967.48	7870.12	10.662	8.53	0.000223
FC-66	−3031.69	6817.71	10.539	−1.35	0.000169
FC-72	−2905.84	4411.29	9.813	0.68	0.000267

The RSS signifies residual sum of squares, $mmol^2/g^2$

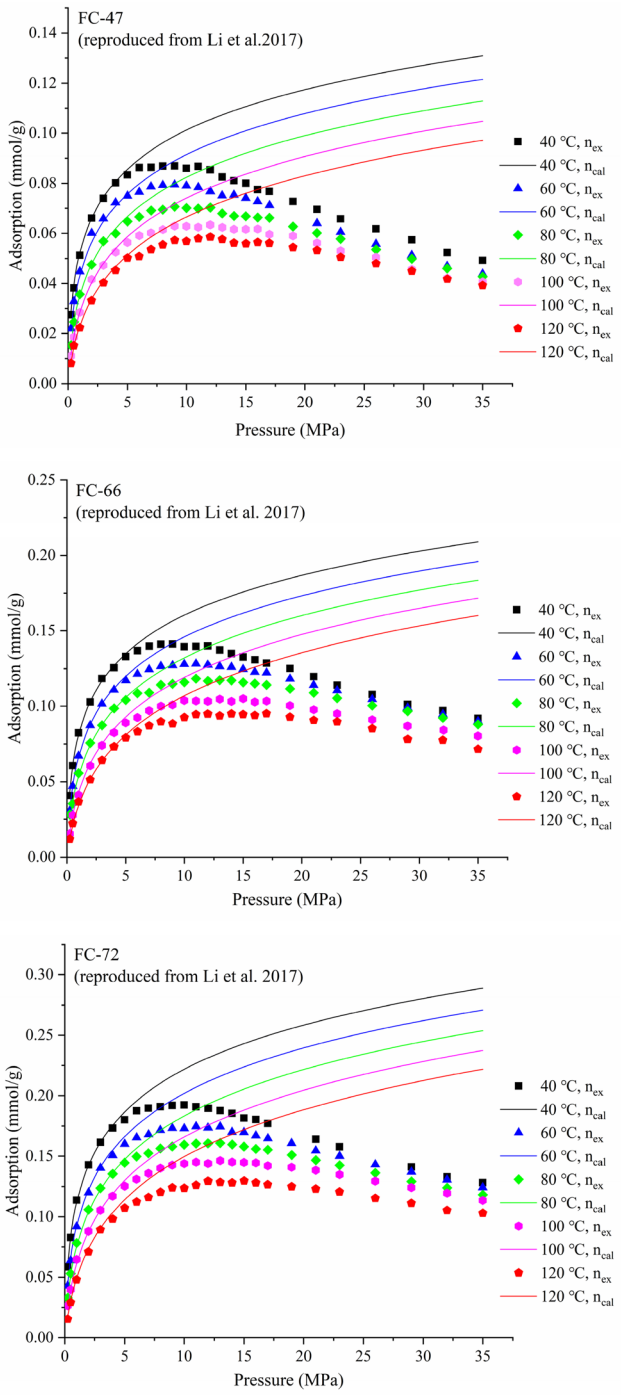

Fig. 1 The fitting of first-order virial equation and methane adsorption on shale between 40 ℃ to 120 ℃. Solid symbols dote the experimental excess adsorption from literature [10]

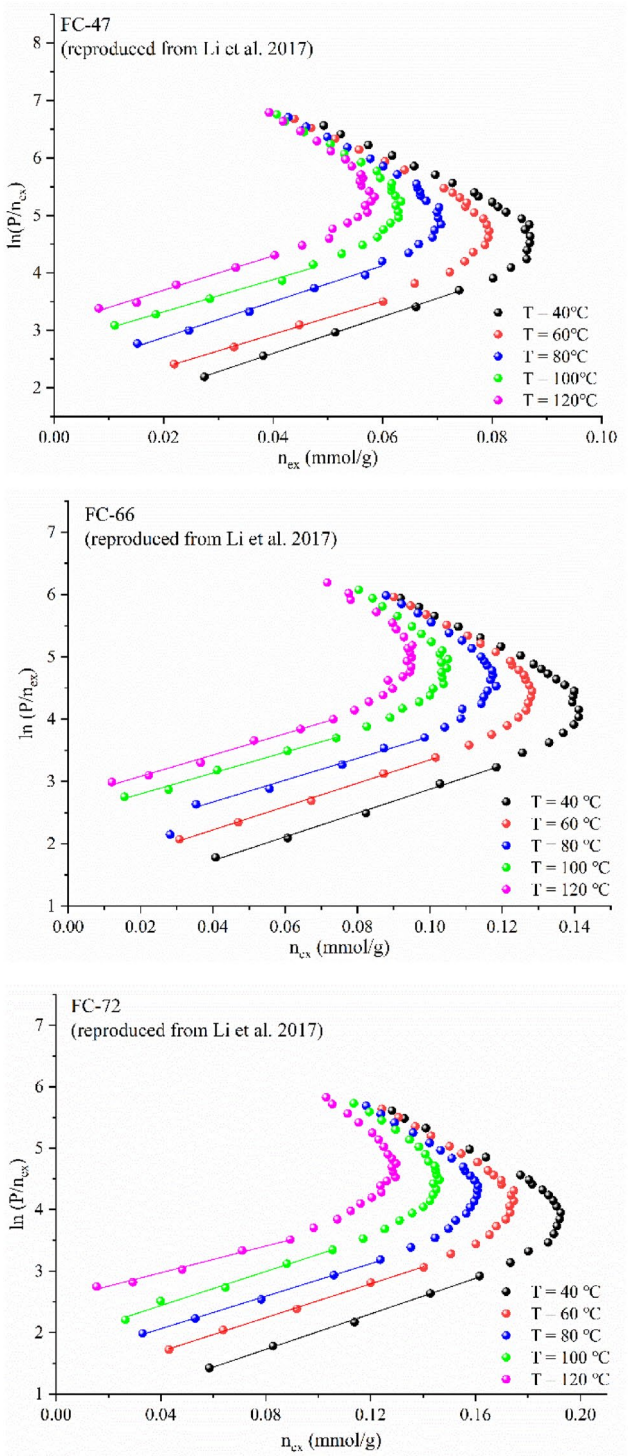

Fig. 2 Virial plots of methane adsorption for samples FC-47, FC-66, and FC-72, data are reproduced from literature [10]. (Note the first data at 80 ℃ of sample FC-66 are excluded because of the large deviation between the measured data and the model fitted data in the original reference)

absolute and excess adsorption is not considerable in this range.

The absolute adsorption (n_{abs}) is known to increase monotonically with increasing pressure for the physisorption system [9]. The smooth curves in Fig. 3 describe the range of n_{abs} are indistinguishable to n_{ex},, all the generalized isotherms in Fig. 3 can be represented by a Langmuir-type equation empirically [39, 49–51]:

Table 3 Fitting results of the virial plots of shale samples

Temperature	FC-47	FC-66	FC-72
40 ℃	y = 31.895x + 1.3245 (R^2 = 0.999); K_H = 0.266	y = 19.094x + 0.9657 (R^2 = 0.996); K_H = 0.3807	y = 14.44x + 0.5711 (R^2 = 0.998); K_H = 0.565
60 ℃	y = 28.869x + 1.7777 (R^2 = 0.999); K_H = 0.169	y = 18.752x + 1.4721 (R^2 = 0.998); K_H = 0.229	y = 13.75 + 1.1427 (R^2 = 0.999); K_H = 0.319
80 ℃	y = 29.547x + 2.2955 (R^2 = 0.997); K_H = 0.100	y = 17.543x + 1.9681 (R^2 = 0.990); K_H = 0.1397	y = 13.24x + 1.5324 (R^2 = 0.998); K_H = 0.216
100 ℃	y = 28.096x + 2.7602 (R^2 = 0.990); K_H = 0.0633	y = 16.749X + 2.4657 (R^2 = 0.992); K_H = 0.0850	y = 14.014x + 1.8769 (R^2 = 0.992); K_H = 0.153
120 ℃	y = 29.942x + 3.0996 (R^2 = 0.989) K_H = 0.045	y = 17.131x + 2.7393 (R^2 = 0.990); K_H = 0.0646	y = 12.504x + 2.4394 (R^2 = 0.993); K_H = 0.087

$$Y = \lambda \frac{bX}{1 + bX} \tag{7}$$

where $Y = \ln\ (1000 \cdot n_{ex})$, $n_{ex} > 0.001$ mmol/g; $X = \ln\ (K_H \cdot P)$, and λ and b are undetermined parameters. Set $E = \ln Y = \ln[\ln(1000 \cdot n_{ex})]$ and $F = 1/bX = 1/[b \cdot \ln(K_H \cdot P)]$, the Eq. 7 can be expressed as:

$$Y = \frac{\lambda}{1 + F} \tag{8}$$

Taking the logarithm on the left- and right-hand sides of Eq. (8):

$$E = \ln Y = \ln \lambda - \ln(1 + F) \tag{9}$$

The $ln\ (1 + F)$ can be expended as a Taylor series:

$$\ln(1 + F) = F - \frac{1}{2}F^2 + \frac{1}{3}F^3 - \cdots + \frac{(-1)^{n+1}}{n}F^n \tag{10}$$

Ignoring the higher order right-hand terms in Eq. (10), because $|F| < 1$, we obtain

$$E = \ln \lambda - F \tag{11}$$

As clearly indicated in Eq. (11), when plotting E (i.e. $ln[ln(1000 \cdot n_{ex})]$) against $1/\ln(K_H \cdot P)$, there must be a linear relationship in the low methane coverage range, namely, the relatively low-pressure range. Absolute adsorption is indistinguishable to excess adsorption in the low methane coverage range because ρ_g is negligible compared with ρ_a. The linear plots in Fig. 4 can be regarded as the absolute adsorption.

Taking $1/ln(P)$ as the X-axis and $ln[ln(1000 \cdot n_{ex})]$ as the Y-axis in the linear region of Fig. 4, the linear plots in Fig. 4 can all be expressed using a linear equation [52]:

$$\ln\left[\ln\left(1000 \cdot n_{ex}\right)\right] = \ln\left[\ln\left(1000 \cdot n_{abs}\right)\right] = \alpha + \frac{\beta}{\ln P} \tag{12}$$

where the α and β are the intercept and slope of the linear equation, respectively. Both α and β can be obtained from linear fitting, see Table 4. From Eq. (12), the absolute adsorption n_{abs} can be expressed as

$$n_{abs} = \frac{1}{1000} \exp\left[\exp\left(\alpha + \frac{\beta}{\ln P}\right)\right] \tag{13}$$

The volume of the adsorbed phase can be derived as:

$$V_a = \frac{n_{abs} - n_{ex}}{\rho_g} \tag{14}$$

The bulk methane density ρ_g in Eq. (14) can be calculated using the REFPROP 9.0 software [53]. To date, the absolute adsorption and the volume of adsorbed phase have been obtained from the foregoing mathematical model. The density of adsorbed phase ρ_a can be evaluated:

$$\rho_a = \frac{n_{abs}}{V_a} = \left(\frac{n_{abs}}{n_{abs} - n_{ex}}\right)\rho_g \tag{15}$$

Hence, this model provides a straightforward approach to evaluate the absolute adsorption, density, and volume of adsorbed phase from the experimental excess adsorption. To validate this model, we compare the parameters obtained from this model with the SDR model [10] and Ono-Kondo model.

The Ono-Kondo model process several advantages and it was introduced for representing gas adsorption on shale successfully [54–56]. The Ono-Kondo model for multilayer adsorption can be expressed as [57]:

$$\ln\left[\frac{X_i(1 - X_b)}{X_b(1 - X_i)}\right] + \left[z_0(X_i - X_b)\right]\frac{E}{kT} + \left[z_2(X_{i+1} - 2X_i + X_{i-1})\right]\frac{E}{kT} = 0, i = 2, 3, \ldots \tag{16}$$

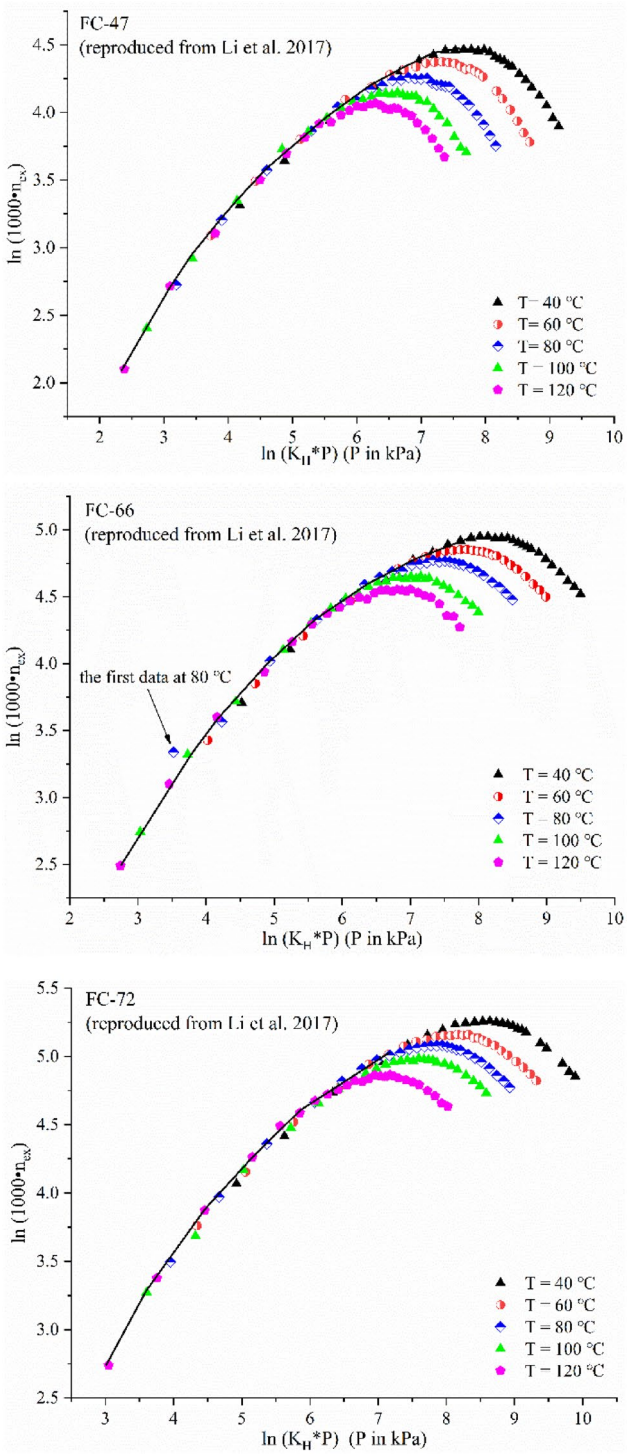

Fig. 3 Generalized isotherms for methane adsorption for samples FC-47, FC-66, and FC-72. Data reproduced from literature [10]

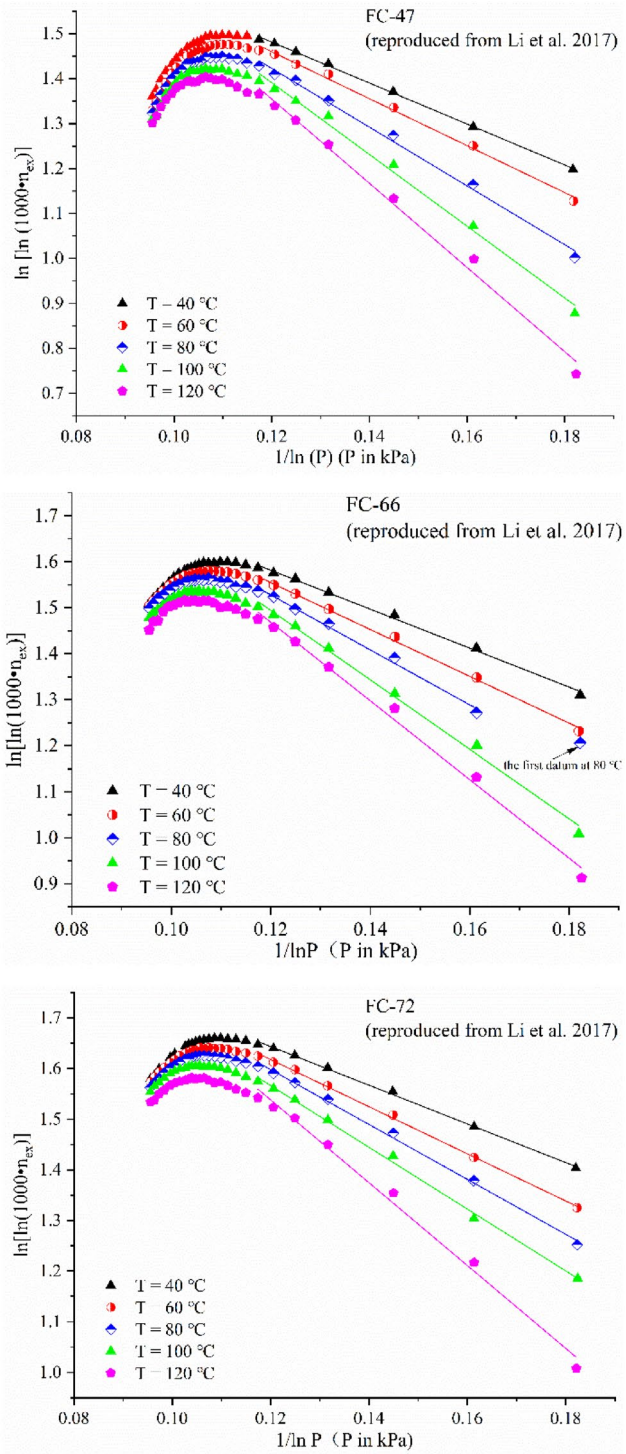

Fig. 4 Linear plots of methane adsorption for samples FC-47, FC-66, and FC-72. Data reproduced from Li et al. [10] (Note the first datum at 80 ℃ of sample FC-66 are excluded because of the large deviation between the measured data and model fitted data in the reference)

Table 4 Fitting parameters for the linear plots in Fig. 3

Sample	FC-47			FC-66			FC-72		
	α	β	R^2	α	B	R^2	α	B	R^2
T = 40 ℃	2.028	−4.5574	0.999	2.0907	−4.2417	0.997	2.1018	−3.8183	0.998
T = 60 ℃	2.0864	−5.2237	0.996	2.1664	−5.0979	0.998	2.1761	−4.653	0.999
T = 80 ℃	2.207	−6.5373	0.994	2.2458	−5.9823	0.994	2.2485	−5.4211	0.997
T = 100 ℃	2.3484	−7.9812	0.993	2.4003	−7.5509	0.995	2.2985	−6.1002	0.997
T = 120 ℃	2.4786	−9.369	0.993	2.4946	−8.5509	0.993	2.4448	−7.5749	0.997

Table 5 Fitting results of the monolayer Ono-Kondo model and RMSE of the shale samples

Sample	T (℃)	C (mmol/g)	E_s/k (K)	E/k (K)	ρ_m (mol/L)	RMSE (mmol/g)
FC-47	40	0.0634	−4.49	0.292	22.53	0.00075
	60	0.0599	−4.23	0.282	20.07	0.00066
	80	0.0554	−3.83	0.237	19.53	0.00062
	100	0.0532	−3.46	0.221	18.06	0.00055
	120	0.0511	−3.13	0.186	17.53	0.00062
FC-66	40	0.1026	−4.56	0.308	25.13	0.00099
	60	0.0978	−4.19	0.284	24.18	0.00067
	80	0.0952	−3.85	0.279	22.85	0.00137
	100	0.0909	−3.42	0.250	20.87	0.00094
	120	0.0883	−3.13	0.241	18.81	0.00104
FC-72	40	0.1394	−4.67	0.326	25.67	0.00099
	60	0.1289	−4.26	0.268	25.11	0.00113
	80	0.1243	−3.98	0.249	23.44	0.00066
	100	0.1181	−3.70	0.236	22.86	0.00086
	120	0.1077	−3.29	0.161	21.48	0.00089

$$\ln\left[\frac{X_1(1-X_b)}{X_b(1-X_1)}\right]+(z_1X_1+z_2X_2-z_0X_b)\frac{E}{kT}+\frac{E_s}{kT}=0,\ i=1 \tag{17}$$

$$X_i=\frac{\rho_i}{\rho_m} \tag{18}$$

$$X_b=\frac{\rho_b}{\rho_m} \tag{19}$$

where X_i is the fraction of occupied adsorption site in the i*th* layer; X_b is the fraction occupied by the bulk phase, and $X_{i+1}=X_b$; ρ_i is the density of adsorbed phase in the i*th* layer; ρ_m is the maximum density of adsorbed phase, namely, the density when all the adsorption site are occupied; k is the Boltzmann constant; z_0 is coordination number in the bulk; z_1 is coordination number within any layer; $z_2=(z_0-z_1)/2$. For a hexagonal configuration of lattice cells, $z_0=8$, $z_1=6$, and $z_2=1$, respectively. E/k indicates the interaction energy of bulk phase, and E_s/k describes the interaction energy of adsorbed gas and pore surface. The excess adsorption is [57]:

$$n_{ex}=2C\sum_{i=1}\left(X_i-X_b\right) \tag{20}$$

where C is a prefactor related to the active sites of the adsorbent for a specific gas. In the Ono-Kondo model, the C, ρ_m, E_s and E are regression parameters.

Recent investigation by applying the Ono-Kondo model have showed that the supercritical methane adsorption on shale is monolayer adsorption [56]. In this study, we apply the monolayer scenario of the Ono-Kondo model to represent the experimental data. Obviously, in the monolayer Ono-Kondo model, the X_2 in Eq. (17) will be replaced as X_b, because the density of the "second layer" equals to the density of bulk methane. The *fslove* in MATLAB was used to solve the nonlinear equations (Eq. 17, Eq. 18, Eq. 19, Eq. 20) and the *lsqcurvefit* in MATLAB was used to fit the experimental data. For monolayer scenario, one can directly obtain the density of adsorbed phase and absolute adsorption via the Ono-Kondo model. We considered the root mean square error (RMSE) [58] to evaluate the disagreement between the model fitted excess adsorption and the experimental results:

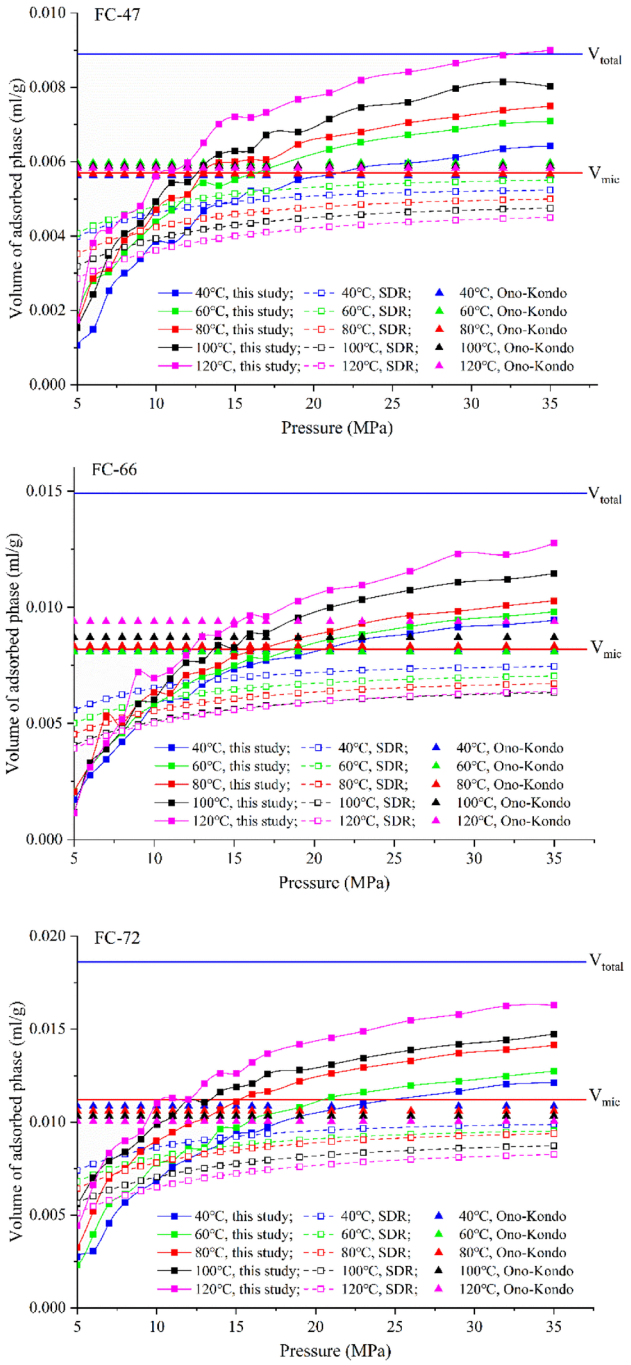

Fig. 5 Volume of adsorbed methane. The solid dots denote the data calculated in this study, whereas the hollow dots denote the data evaluated in the original literature [10]. V_{taotal} signifies the total pore volume evaluated from the N_2 adsorption/desorption; V_{mic} denotes the pore volume of micropores determined from CO_2 adsorption. The lines are included for better traceability

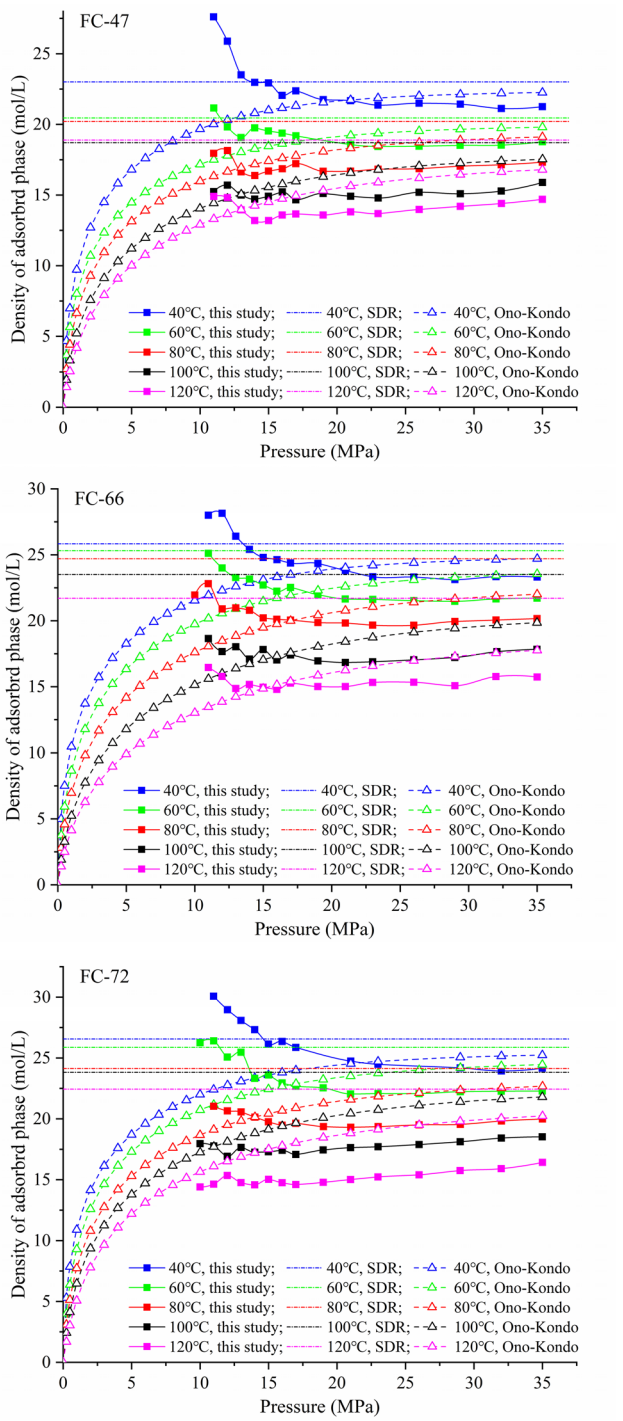

Fig. 6 Density of adsorbed methane for three shale samples at different temperatures, reproduced from literature [10]. The horizontal dashed lines denote the adsorbed density of methane evaluated by the SDR model

$$RMSE = \sqrt{\frac{1}{m}\sum_{i=1}^{m}(n_{cal} - n_{ex})^2} \tag{21}$$

where n_{cal} is the adsorbed quantity calculated using the model and m is the number of experimental data at a given temperature.

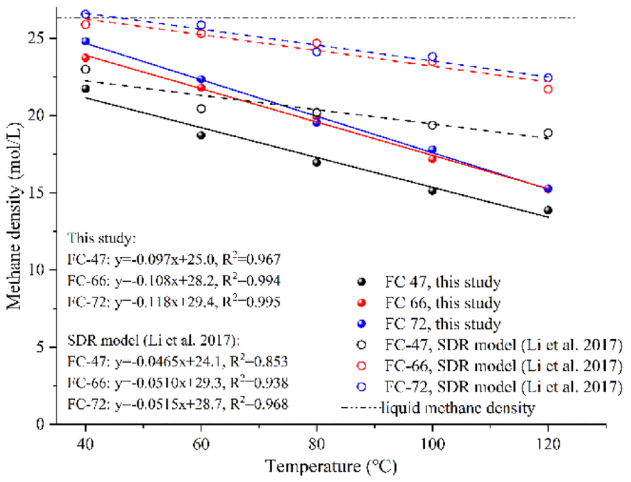

Fig. 7 Average densities of the adsorbed methane calculated at pressures above 15 MPa and adsorbed methane densities from literature (The colored spheres represent the data from this study, whereas the hollow circles denote data from literature [10]. The dot-dashed line denotes the liquid methane density at the boiling point (26.35 mol/L at -162 ℃))

3 Results and discussion

3.1 Excess adsorption isotherms

The model evaluation results verify that both the monolayer Ono-Kondo model and the SDR model can represent methane adsorption; the monolayer Ono-Kondo model has an RMSE below 0.00137 mmol/g (Table 5), which is equivalent to the original SDR model (Eq. 22) based on the assumption that the unknown adsorbed density is constant. The interaction energy of adsorbed gas and pore surface (E_s/k) is negative, indicating the attractive force. However, the interaction energy of bulk phase (E/k) is positive, indicating the bulk methane has repulsive force among molecules. The absolute value of E_s/k and E/k decline with increasing temperature indicating that attractive effect between the methane and pore surface and the repulsive effect among the bulk gas molecules decrease. The parameter C also declines with increasing temperature implying that some of the adsorption sites will lose the methane molecules under higher temperature, resulting in the decline in maximum density ρ_m.

$$n_{ex} = n_{\infty}\left\{-D\left[\ln\left(\frac{\rho_a}{\rho_g}\right)RT\right]^2\right\}\left(1-\frac{\rho_g}{\rho_a}\right) \tag{22}$$

$$n_{abs} = n_{\infty}\left\{-D\left[\ln\left(\frac{\rho_a}{\rho_g}\right)RT\right]^2\right\} \tag{23}$$

Here n_{∞} signifies the maximum absolute adsorption capacity of micropore-filling; D is a pore structure parameter. In the SDR model, n_{∞}, ρ_a are temperature-dependent fitting parameters and D is temperature-independent fitting parameter [10].

3.2 Adsorbed methane density and volume

As both the adsorbed methane volume and adsorbed methane density have remained unmeasurable, it is imperative to develop a robust method to estimate the adsorbed methane volume and adsorbed methane density. The model adopted in this study provides information on the absolute adsorption firstly and the adsorbed phase volume, and the adsorbed phase density can be evaluated from Eq. (14) and Eq. (15), respectively. The adsorbed methane volume as a function of the temperature and pressure is depicted in Fig. 5. As the uncertainty in the volume evaluated using Eq. (14) is considerably higher at relatively low pressure than that in the relatively high-pressure range, to better demonstrate the trend of the adsorbed volume, only parts of the volume are displayed in Fig. 5 for pressures above 5 MPa. This is due to the low bulk methane density ρ_g at relatively low pressure; any small difference between the determined excess adsorption and absolute adsorption can lead to large deviations in the adsorbed methane volume. The adsorbed methane volume increases steeply at moderate pressure and approaches the maximum value. Additionally, the adsorbed phase volume expands slightly with increasing temperate; this is mainly attributable to the liquid-like characteristic of the adsorbed phase [59]. Interestingly, the adsorbed volumes of these three samples are fall between their micropore volumes V_{mic} (horizontal red solid line in Fig. 5) and their total pore volumes V_{total} (horizontal blue solid line in Fig. 5) [10]. Notably, the routinely applied SDR model with the assumption of constant adsorbed phase density overestimated and underestimated the volume of adsorbed methane at low and high pressure, respectively. Therefore, the volumes of adsorbed phase calculated by the SDR model are all smaller than the micropore volumes V_{mic}. Another interesting finding is that the volumes of the adsorbed phase calculated by using the monolayer Ono-Kondo model (solid triangles in Fig. 5) remain constant with increasing pressure and are numerically close to the micropore volumes V_{mic}. Analogously, the assumption that the volume of adsorbed methane is a constant regardless of the temperature and pressure also leads to an inaccurate estimation of the adsorption capacity of methane.

The uncertainty of ρ_a is magnified because the difference between n_{abs} and n_{ex} is negligible at low pressure region. It is difficult to determine a reasonable value for ρ_a at relatively low pressure because (n_{abs}-n_{ex}) is present in the denominator of Eq. (15) [58]. However, the value of ρ_a at high pressure is more reliable and is nearly constant (Fig. 6). As illustrated in Fig. 6, the adsorbed methane density exhibits a

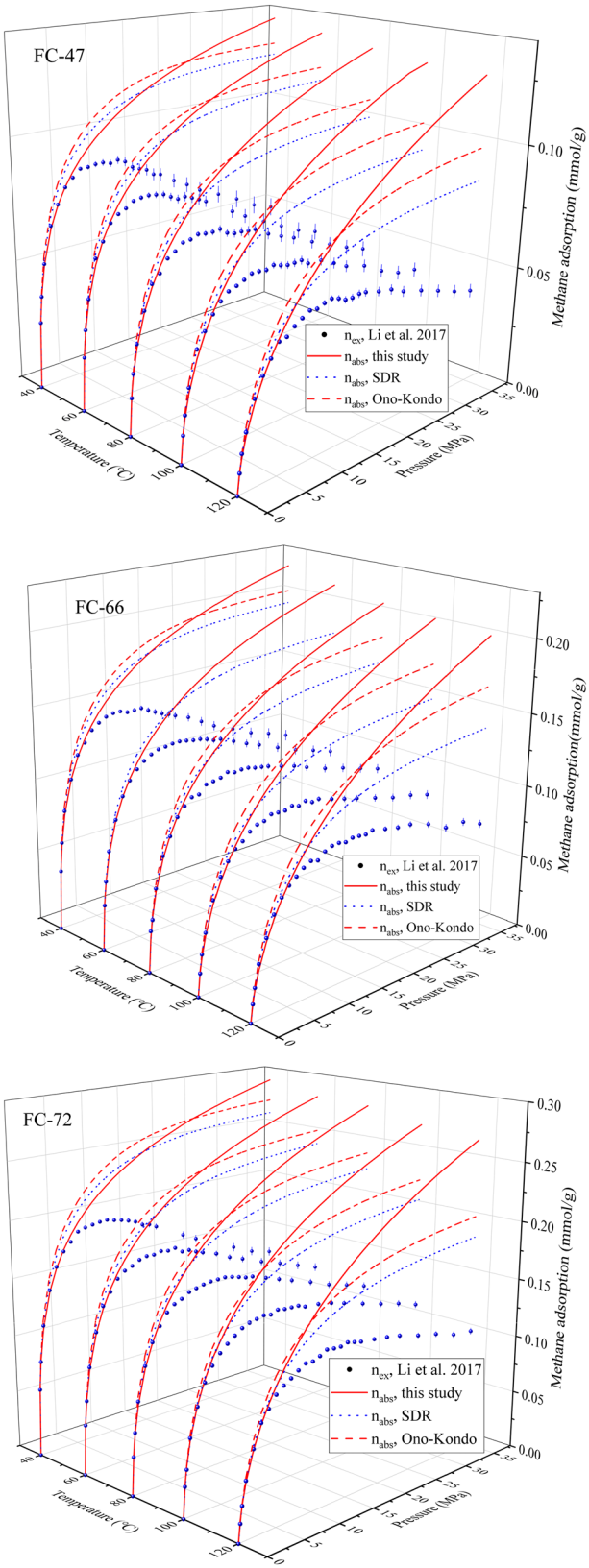

Fig. 8 Absolute adsorption of methane in three shales (The blue spheres denote data extrapolated from the corresponding measured data, the blue dashed lines denote data calculated using the SDR model [10], the red dash lines donate data calculated using the monolayer Ono-Kondo model, and the solid line denotes the data evaluated in this study)

slight reduction above 10 MPa and most of the values are lower than the liquid methane density at the boiling point (26.35 mol/L at -162 ℃), which is widely accepted as the upper limit of the adsorbed density [60, 61]. The slight reduction of the adsorbed phase density might be attributable to the preferential adsorption at different pressures. At low pressure, the methane molecules are preferentially adsorbed on the surfaces of micropores with higher potential. At a given pressure, the adsorbed phase density in the micropores is higher than that in the mesopores [27]. As the pressure increases, the methane molecules are adsorbed on the surface of fine-mesopores which causes the adsorbed density to decrease slightly. At the same temperature, the densities of adsorbed phase at pressure above 15 MPa are arranged from largest to smallest in the order of the SDR model, the monolayer Ono-Kondo model, and evaluated in this study.

The average values of the adsorbed density of methane at pressures above 15 MPa are plotted in Fig. 7, which shows that all the calculated densities are lower than the liquid methane density (26.35 mol/L at -162 ℃). The adsorbed methane density obtained using the SDR model is always higher than all the density values obtained in this study. In all models, the density decreases linearly with the temperature. This is attributable to the decrease in absolute adsorption and the increase in the adsorbed methane volume with increasing temperature and to the reduction in the density of the liquid-like adsorbed phase with increasing temperature.

3.3 Absolute methane adsorption

It is essential to evaluate shale gas reservoir accurately and acquire more knowledge on methane transport in shale micropores. In nanometer-diameter pores, in particular, surface diffusion of the adsorbed methane can be the main contributor to the total methane flux [62, 63]. Considering methane transport in kerogen pores as an example, the contribution of the adsorbed layer will be more than 60% of the total mass flux, when the pore diameter is less than 2 nm [64]. The absolute adsorption forecast using Eq. (13) and that obtained using the original SDR model from literature [10] and the monolayer Ono-Kondo model are depicted in Fig. 8. In all the cases, the absolute adsorption decreases as the temperature increase because adsorption is an exothermic process.

At a relatively low-pressure range, both the SDR model, the monolayer Ono-Kondo model and the model adopted in this study can represent excess adsorption, which is consistent with the fact that absolute and excess adsorption are approximately identical; however, absolute adsorption increases throughout the entire pressure range. At a higher pressure range, absolute adsorption is consistently higher than the corresponding experimentally measured values. The routinely adopted SDR model with constant adsorbed methane density and the monolayer Ono-Kondo model with constant adsorbed volume underestimate absolute adsorption under high pressure. This inconformity in the absolute adsorption is primarily caused by (i) the SDR and the monolayer Ono-Kondo model's underestimation of the adsorbed methane volume at high pressures, and (ii) calculation of absolute adsorption as the sum of the excess and the product of the adsorbed phase volume and bulk methane density.

4 Conclusions

In this study, a series of methane adsorption isotherms at pressures of up to 35 MPa and temperatures of up to 120 ℃ were analyzed using a mathematical method. This method evaluates absolute adsorption on the basis that absolute and excess adsorption are approximately equivalent at relatively low pressure and then increase over the entire pressure range. This model can estimate the adsorbed phase volume, adsorbed phase density, and absolute adsorption from experimental adsorption data. The main results can be summarized as follows:

1. A mathematical framework provides an alternative method to evaluate high-pressure methane adsorption isotherms (up to 35 MPa and 120 ℃) for three Niutitang shales in Guizhou Province, China with a variational adsorbed density and adsorbed volume with temperature and pressure. The absolute adsorption, adsorbed volume and adsorbed density can be evaluated from the experimental excess data.

2. The adsorbed methane volume increased rapidly in the moderate pressure range and approached a maximum at high-pressure. For all the samples, the adsorbed methane volume expanded slightly as temperature increased, and the adsorbed methane volumes fall into the range of the micropore volume and total pore volume.

3. The adsorbed methane density decreased at pressures above 5 MPa and approached a constant at high pressure. The density at high pressure was lower than the liquid density of methane at its boiling temperature. The SDR-based model with a constant adsorbed phase density and the monolayer Ono-Kondo model overestimated the adsorbed phase density and underestimated the adsorbed volume and absolute adsorption at high pressure region.

Acknowledgements The first author expresses his gratitude to the China Scholarship Council (no. 201406050029) and thanks Prof. Hui Tian at the Guangzhou Institute of Geochemistry, Chinese Academy of Sciences, for providing methane adsorption data.

Funding Open Access funding enabled and organized by Projekt DEAL. This study is partly supported by the China Scholarship Council (no.201406050029). Chinese Government Scholarship,201406050029,Ke Hu

Data availability The data that support the findings of this study are available on request from the corresponding author.

Declarations

Conflict of interest The authors declare no conflict of interest.

References

1. Arogundade, O., Sohrabi, M.: A review of recent developments and challenaes in shale gas recovery. In: Society of Petroleum Engineers - SPE Saudi Arabia Section Technical Symposium and Exhibition 2012 (2012)
2. EIA Energy Outlook 2020. , Washington (2019)
3. Curtis, J.B.: Fractured shale-gas systems. Am. Assoc. Pet. Geol. Bull. (2002)
4. Montgomery, S.L., Jarvie, D.M., Bowker, K.A., Pollastro, R.M.: Mississippian Barnett Shale, Fort Worth basin, north-central Texas: Gas-shale play with multi-trillion cubic foot potential. Am. Assoc. Pet. Geol. Bull. (2005). https://doi.org/10.1306/09170404042
5. Gasparik, M., Ghanizadeh, A., Bertier, P., Gensterblum, Y., Bouw, S., Krooss, B.M.: High-pressure methane sorption isotherms of black shales from the Netherlands. Energy Fuels **26**, 4995–5004 (2012). https://doi.org/10.1021/ef300405g
6. Gasparik, M., Bertier, P., Gensterblum, Y., Ghanizadeh, A., Krooss, B.M., Littke, R.: Geological controls on the methane storage capacity in organic-rich shales. Int. J. Coal Geol. (2014). https://doi.org/10.1016/j.coal.2013.06.010
7. Merkel, A., Fink, R., Littke, R.: High pressure methane sorption characteristics of lacustrine shales from the Midland Valley Basin. Scotland. Fuel. **182**, 361–372 (2016). https://doi.org/10.1016/j.fuel.2016.05.118
8. Pan, L., Xiao, X., Tian, H., Zhou, Q., Cheng, P.: Geological models of gas in place of the Longmaxi shale in Southeast Chongqing. South China. Mar. Pet. Geol. (2016). https://doi.org/10.1016/j.marpetgeo.2016.03.018
9. Tang, X., Ripepi, N., Stadie, N.P., Yu, L., Hall, M.R.: A dual-site Langmuir equation for accurate estimation of high pressure deep

shale gas resources. Fuel **185**, 10–17 (2016). https://doi.org/10.1016/j.fuel.2016.07.088
10. Li, T., Tian, H., Xiao, X., Cheng, P., Zhou, Q., Wei, Q.: Geochemical characterization and methane adsorption capacity of overmature organic-rich Lower Cambrian shales in northeast Guizhou region, southwest China. Mar. Pet. Geol. (2017). https://doi.org/10.1016/j.marpetgeo.2017.06.043
11. Shabani, M., Moallemi, S.A., Krooss, B.M., Amann-Hildenbrand, A., Zamani-Pozveh, Z., Ghalavand, H., Littke, R.: Methane sorption and storage characteristics of organic-rich carbonaceous rocks, Lurestan province, southwest Iran. Int. J. Coal Geol. (2018). https://doi.org/10.1016/j.coal.2017.12.005
12. Li, J., Zhou, S., Gaus, G., Li, Y., Ma, Y., Chen, K., Zhang, Y.: Characterization of methane adsorption on shale and isolated kerogen from the Sichuan Basin under pressure up to 60 MPa: experimental results and geological implications. Int. J. Coal Geol. (2018). https://doi.org/10.1016/j.coal.2018.02.020
13. Hu, K., Mischo, H.: Modeling high-pressure methane adsorption on shales with a simplified local density model. ACS Omega. **5**, 5048–5060 (2020). https://doi.org/10.1021/acsomega.9b03978
14. Langmuir, I.: The adsorption of gases on plane surfaces of glass, mica and platinum. J. Am. Chem. Soc. (1918). https://doi.org/10.1021/ja02242a004
15. Dubinin, M.M.: Fundamentals of the theory of adsorption in micropores of carbon adsorbents: characteristics of their adsorption properties and microporous structures. Carbon N. Y. (1989). https://doi.org/10.1016/0008-6223(89)90078-X
16. Clarkson, C.R., Solano, N., Bustin, R.M., Bustin, A.M.M., Chalmers, G.R.L., He, L., Melnichenko, Y.B., Radliński, A.P., Blach, T.P.: Pore structure characterization of North American shale gas reservoirs using USANS/SANS, gas adsorption, and mercury intrusion. Fuel **103**, 606–616 (2013). https://doi.org/10.1016/j.fuel.2012.06.119
17. Al Hinai, A., Rezaee, R., Esteban, L., Labani, M.: Comparisons of pore size distribution: a case from the Western Australian gas shale formations. J. Unconv. Oil Gas Resour. **8**, 1–13 (2014). https://doi.org/10.1016/j.juogr.2014.06.002
18. Klaver, J., Desbois, G., Urai, J.L., Littke, R.: BIB-SEM study of the pore space morphology in early mature Posidonia Shale from the Hils area. Germany. Int. J. Coal Geol. **103**, 12–25 (2012). https://doi.org/10.1016/j.coal.2012.06.012
19. Li, J., Yin, J., Zhang, Y., Lu, S., Wang, W., Li, J., Chen, F., Meng, Y.: A comparison of experimental methods for describing shale pore features - a case study in the Bohai Bay Basin of eastern China. Int. J. Coal Geol. **152**, 39–49 (2015). https://doi.org/10.1016/j.coal.2015.10.009
20. Saraji, S., Piri, M.: The representative sample size in shale oil rocks and nano-scale characterization of transport properties. Int. J. Coal Geol. **146**, 42–54 (2015). https://doi.org/10.1016/j.coal.2015.04.005
21. Slatt, R.M., O'Brien, N.R.: Pore types in the Barnett and Woodford gas shales: contribution to understanding gas storage and migration pathways in fine-grained rocks. Am. Assoc. Pet. Geol. Bull. **95**, 2017–2030 (2011). https://doi.org/10.1306/03301110145
22. Sun, M., Yu, B., Hu, Q., Chen, S., Xia, W., Ye, R.: Nanoscale pore characteristics of the lower Cambrian Niutitang formation shale: a case study from well Yuke #1 in the Southeast of Chongqing. China. Int. J. Coal Geol. (2016). https://doi.org/10.1016/j.coal.2015.11.015
23. Wei, M., Zhang, L., Xiong, Y., Li, J., Peng, P.: Nanopore structure characterization for organic-rich shale using the non-local-density functional theory by a combination of N2and CO2adsorption. Microporous Mesoporous Mater. **227**, 88–94 (2016). https://doi.org/10.1016/j.micromeso.2016.02.050
24. Yan, G., Li, X., Guo, W., Zhou, S., Xue, H.: 2D and 3D nanopore characterization of gas shale in Longmaxi formation based on FIB-SEM. Mar. Pet. Geol. **73**, 174–180 (2016). https://doi.org/10.1016/j.marpetgeo.2016.02.033
25. Murata, K., El-Merraoui, M., Kaneko, K.: A new determination method of absolute adsorption isotherm of supercritical gases under high pressure with a special relevance to density-functional theory study. J. Chem. Phys. **114**, 4196–4205 (2001). https://doi.org/10.1063/1.1344926
26. Tang, X., Ripepi, N., Luxbacher, K., Pitcher, E.: Adsorption models for methane in shales: review, comparison, and application. Energy Fuels **31**, 10787–10801 (2017). https://doi.org/10.1021/acs.energyfuels.7b01948
27. Mosher, K., He, J., Liu, Y., Rupp, E., Wilcox, J.: Molecular simulation of methane adsorption in micro- and mesoporous carbons with applications to coal and gas shale systems. Int. J. Coal Geol. (2013). https://doi.org/10.1016/j.coal.2013.01.001
28. Do, D.D., Do, H.D.: Adsorption of argon from sub- to supercritical conditions on graphitized thermal carbon black and in graphitic slit pores: a grand canonical monte Carlo simulation study. J. Chem. Phys. **123**, 1–15 (2005). https://doi.org/10.1063/1.1996573
29. Humayun, R., Tomasko, D.L.: High-resolution adsorption isotherms of supercritical carbon dioxide on activated carbon. AIChE J. (2000). https://doi.org/10.1002/aic.690461017
30. Zou, C., Dong, D., Wang, Y., Li, X., Huang, J., Wang, S., Guan, Q., Zhang, C., Wang, H., Liu, H., Bai, W., Liang, F., Lin, W., Zhao, Q., Liu, D., Yang, Z., Liang, P., Sun, S., Qiu, Z.: Shale gas in China: characteristics, challenges and prospects (I). Pet. Explor. Dev. **42**, 753–767 (2015). https://doi.org/10.1016/S1876-3804(15)30072-0
31. Zou, C., Dong, D., Wang, Y., Li, X., Huang, J., Wang, S., Guan, Q., Zhang, C., Wang, H., Liu, H., Bai, W., Liang, F., Lin, W., Zhao, Q., Liu, D., Yang, Z., Liang, P., Sun, S., Qiu, Z.: Shale gas in China: characteristics, challenges and prospects (II). Pet. Explor. Dev. **43**, 182–196 (2016). https://doi.org/10.1016/S1876-3804(16)30022-2
32. Zou, C., Du, J., Xu, C., Wang, Z., Zhang, B., Wei, G., Wang, T., Yao, G., Deng, S., Liu, J., Zhou, H., Xu, A., Yang, Z., Jiang, H., Gu, Z.: Formation, distribution, resource potential, and discovery of Sinian-Cambrian giant gas field, Sichuan Basin. SW China. Pet. Explor. Dev. **41**, 306–325 (2014). https://doi.org/10.1016/S1876-3804(14)60036-7
33. Lin, K., Huang, X., Zhao, Y.P.: Combining image recognition and simulation to reproduce the adsorption/desorption behaviors of shale gas. Energy Fuels **34**, 258–269 (2020). https://doi.org/10.1021/acs.energyfuels.9b03669
34. Chareonsuppanimit, P., Mohammad, S.A., Robinson, R.L., Gasem, K.A.M.: High-pressure adsorption of gases on shales: measurements and modeling. Int. J. Coal Geol. **95**, 34–46 (2012). https://doi.org/10.1016/j.coal.2012.02.005
35. Charoensuppanimit, P., Mohammad, S.A., Robinson, R.L., Gasem, K.A.M.: Modeling the temperature dependence of supercritical gas adsorption on activated carbons, coals and shales. Int. J. Coal Geol. **138**, 113–126 (2015). https://doi.org/10.1016/j.coal.2014.12.008
36. Pang, Y., Soliman, M.Y., Sheng, J.: Investigation of adsorption effects on nanopores in shale gas reservoir by simplified local-density model. In: SPE/AAPG/SEG Unconventional Resources Technology Conference 2016 (2016)
37. Zuo, L., Rui, S., Guo, W., Hu, Z., Wang, Y., Gao, S., Xiong, W.: Methane adsorption on shale: insights from experiments and a simplified local density model. Adsorpt. Sci. Technol. **32**, 535–556 (2014). https://doi.org/10.1260/0263-6174.32.7.535
38. Brandani, S., Mangano, E., Sarkisov, L.: Net, excess and absolute adsorption and adsorption of helium. Adsorption **22**, 261–276 (2016). https://doi.org/10.1007/s10450-016-9766-0

39. Stadie, N.P., Murialdo, M., Ahn, C.C., Fultz, B.: Anomalous isosteric enthalpy of adsorption of methane on zeolite-templated carbon. J. Am. Chem. Soc. (2013). https://doi.org/10.1021/ja311415m
40. Cai, H., Li, P., Ge, Z., Xian, Y., Lu, D.: A new method to determine varying adsorbed density based on Gibbs isotherm of supercritical gas adsorption. Adsorpt. Sci. Technol. (2018). https://doi.org/10.1177/0263617418802665
41. Pini, R.: Interpretation of net and excess adsorption isotherms in microporous adsorbents. Microporous Mesoporous Mater. (2014). https://doi.org/10.1016/j.micromeso.2013.12.005
42. Ottiger, S., Pini, R., Storti, G., Mazzotti, M.: Competitive adsorption equilibria of CO2 and CH4 on a dry coal. Adsorption (2008). https://doi.org/10.1007/s10450-008-9114-0
43. Hwang, J., Joss, L., Pini, R.: Measuring and modelling supercritical adsorption of CO2 and CH4 on montmorillonite source clay. Microporous Mesoporous Mater. (2019). https://doi.org/10.1016/j.micromeso.2018.06.050
44. Hwang, J., Pini, R.: Supercritical CO2 and CH4 uptake by Illite-Smectite Clay Minerals. Environ. Sci. Technol. (2019). https://doi.org/10.1021/acs.est.9b03638
45. Himeno, S., Tomita, T., Suzuki, K., Yoshida, S.: Characterization and selectivity for methane and carbon dioxide adsorption on the all-silica DD3R zeolite. Microporous Mesoporous Mater. (2007). https://doi.org/10.1016/j.micromeso.2006.05.018
46. Wang, Y., Helvensteijn, B., Nizamidin, N., Erion, A.M., Steiner, L.A., Mulloth, L.M., Luna, B., Levan, M.D.: High pressure excess isotherms for adsorption of oxygen and nitrogen in zeolites. Langmuir (2011). https://doi.org/10.1021/la201690x
47. D.M.Ruthven: Principles of adsorption and adsorption processes. (1984)
48. Zhou, L., Zhang, J., Zhou, Y.: A simple isotherm equation for modeling the adsorption equilibria on porous solids over wide temperature ranges. Langmuir (2001). https://doi.org/10.1021/la010005p
49. Zhou, L., Bai, S., Su, W., Yang, J., Zhou, Y.: Comparative study of the excess versus absolute adsorption of CO2 on superactivated carbon for the near-critical region. Langmuir (2003). https://doi.org/10.1021/la020682z
50. Zhou, L., Zhou, Y.: 2001 A mathematical method for determination of absolute adsorption from experimental isotherms of supercritical gases. Chinese J. Chem. Eng.
51. Zhou, L., Zhou, Y., Li, M., Chen, P., Wang, Y.: Experimental and modeling study of the adsorption of supercritical methane on a high surface activated carbon. Langmuir (2000). https://doi.org/10.1021/la991159w
52. Zhou, L., Zhou, Y.: Linearization of adsorption isotherms for high-pressure applications. Chem. Eng. Sci. (1998). https://doi.org/10.1016/S0009-2509(98)00065-7
53. Lemmon, E.W., Huber, M.L., McLinden, M.O.: NIST Standard Reference Database 23: Reference Fluid Thermodynamic and Transport Properties (REFPROP), Version 9.0. Phys. Chem. Prop. …. (2010)
54. Merey, S., Sinayuc, C.: Analysis of carbon dioxide sequestration in shale gas reservoirs by using experimental adsorption data and adsorption models. J. Nat. Gas Sci. Eng. (2016). https://doi.org/10.1016/j.jngse.2016.02.052
55. Pang, W., Jin, Z.: Ono-Kondo lattice model for propane multilayer adsorption in organic nanopores in relation to shale gas. Fuel **235**, 158–166 (2019). https://doi.org/10.1016/j.fuel.2018.07.086
56. Xiong, F., Rother, G., Tomasko, D., Pang, W., Moortgat, J.: On the pressure and temperature dependence of adsorption densities and other thermodynamic properties in gas shales. Chem. Eng. J. (2020). https://doi.org/10.1016/j.cej.2020.124989
57. Sudibandriyo, M., Mohammad, S.A., Robinson, R.L., Jr., Gasem, K.A.M.: Ono-Kondo lattice model for high-pressure adsorption: pure gases. Fluid Phase Equilib. (2010). https://doi.org/10.1016/j.fluid.2010.09.032
58. Fitzgerald, J.E., Pan, Z., Sudibandriyo, M., Robinson, R.L., Gasem, K.A.M., Reeves, S.: Adsorption of methane, nitrogen, carbon dioxide and their mixtures on wet Tiffany coal. Fuel (2005). https://doi.org/10.1016/j.fuel.2005.05.002
59. Srinivasan, K., Saha, B.B., Ng, K.C., Dutta, P., Prasad, M.: A method for the calculation of the adsorbed phase volume and pseudo-saturation pressure from adsorption isotherm data on activated carbon. Phys. Chem. Chem. Phys. (2011). https://doi.org/10.1039/c1cp20383e
60. Do, D.D., Do, H.D.: Adsorption of supercritical fluids in non-porous and porous carbons: analysis of adsorbed phase volume and density. Carbon N. Y. (2003). https://doi.org/10.1016/S0008-6223(03)00152-0
61. Hu, K., Mischo, H.: High-pressure methane adsorption and desorption in shales from the sichuan basin. Southwestern China. Energy & Fuels. **34**, 2945–2957 (2020). https://doi.org/10.1021/acs.energyfuels.9b04142
62. Swami, V., Settari, A.: A Pore Scale Gas Flow Model for Shale Gas Reservoir. (2012). https://doi.org/10.2118/155756-ms
63. Wu, K., Li, X., Guo, C., Wang, C., Chen, Z.: A unified model for gas transfer in nanopores of shale-gas reservoirs: Coupling pore diffusion and surface diffusion. In: SPE Journal (2016)
64. Ren, J., Guo, P., Guo, Z., Wang, Z.: A lattice Boltzmann model for simulating gas flow in kerogen pores. Transp. Porous Media. (2015). https://doi.org/10.1007/s11242-014-0401-9